Topological spin textures in 1*T*-phase Janus magnets: Interplay between Dzyaloshinskii-Moriya interaction, magnetic frustration, and isotropic higher-order interactions

Peng Li,[1,2] Dongxing Yu,[1] Jinghua Liang,[1] Yonglong Ga,[1,2] and Hongxin Yang ●[1,3,*]

[1]*Ningbo Institute of Materials Technology and Engineering, Chinese Academy of Sciences, Ningbo 315201, China*
[2]*Center of Materials Science of Optoelectronics Engineering, University of Chinese Academy of Sciences, Beijing 100049 China*
[3]*National Laboratory of Solid State Microstructures, School of Physics, Collaborative Innovation Center of Advanced Microstructures, Nanjing University, Nanjing 210093, China*

The search for topological magnetism in two-dimensional (2D) magnetic materials is one of the hot topics in spintronics. We present comprehensive studies of magnetic phases in a series of Janus monolayers MnXZ (MnAsBr, MnAsI, MnPBr, and MnPCl) and CrYZ (Y = Se, Te; and Z = Cl, Br, I) via combining first-principles calculations and atomistic spin model simulations. Sizable Dzyaloshinskii-Moriya interaction can be realized in the MnXZ and CrYZ monolayers due to their intrinsic inversion symmetry breaking. More interestingly, the MnXZ and CrYZ monolayers exhibit different degrees of magnetic frustration and isotropic higher-order interactions. Lastly, our atomistic spin model simulations demonstrate that a variety of topological spin textures can be generated by the interplay among complex magnetic interactions. These results provide valuable information and fundamental understanding for topological magnetism in 2D magnets.

I. INTRODUCTION

Magnetic skyrmions [1–4] and bimerons [5–7] are promising candidates for information carriers in next-generation spintronic devices due to their inert robustness against small external perturbation. These topologically protected spin swirls can be induced by Dzyaloshinskii-Moriya interaction (DMI) [8,9], a spin-orbit coupling (SOC) effect which requires inversion symmetry breaking in magnets. DMI favors rotation of magnetization directions with certain helicity and chirality. Skyrmions of Bloch type, Néel type, and antiskyrmions can be found in acentric B20 materials [3,10], magnetic hetereostructure thin films [2,11–16], and acentric two-dimensional (2D) magnets [17–24] depending on the helicity and chirality of respective DMI. Alternatively, the canting among neighboring spins caused by magnetic frustration and dipole-dipole interactions [25] can also stabilize skyrmionic structures.

Recent experiments show that skyrmions can be formed by the competing nearest-neighbor (NN) ferromagnetic and further neighbor antiferromagnetic Heisenberg exchanges in centrosymmetric bulk materials [26–28]. For centrosymmetric 2D magnets such as the 3*d* metal dihalides [29,30] and trihalides [31,32], the presence of magnetic frustration is ubiquitous. Skyrmions induced by frustration are usually smaller in size [33–38], but the helicity and chirality could be randomly distributed [39].

Apart from DMI and frustration, the isotropic higher-order interactions (HOIs) [14,40–45], especially the four-spin-four-site interaction, could also be important factors for stabilizing skyrmions in the ferromagnetic monolayer/heavy metal systems [14]. Arising from a multiple-electron hopping process between 2–4 atomic sites, the HOI terms (up to the fourth-order approximation) consist of biquadratic, four-spin-three-site, and four-spin-four-site interactions. In the emergent field of 2D magnets, some studies focus on the effect from biquadratic interaction [46–50]. Interestingly, in the Fe$_3$GeTe$_2$ monolayer with vanishing long-range DMI, complex noncollinear magnetism could be formed due to the interplay between magnetic frustration, HOI [50], and short-range DMI components [51]. For acentric magnets, the morphology of topological magnetism can be affected by magnetic anisotropy, DMI, magnetic frustration, and HOIs. In view of optimizing topological spin textures hosting materials, systematic study on the interplay among the aforementioned interactions is necessary.

Herein, from first-principles calculations, we propose four Janus magnetic monolayers MnXZ (MnAsI, MnAsBr, MnPBr, and MnPCl). Next, we determine the magnetic parameters of MnXZ and the previously reported Janus magnets CrYZ (Y = Se, Te; and Z = Cl, Br, I) [52,53], including the respective DMI vectors and Heisenberg exchange interactions up to the third neighbor (NNNN), as well as the values of isotropic HOIs. We identify different frustration and DMI ratios in the monolayers to better understand the interplay between DMI and magnetic frustration in MnXZ and CrYZ monolayers. Furthermore, from atomistic spin model simulations, we find that a variety of topological spin textures can be generated in MnXZ and CrYZ, from which we investigate the impact from different degrees of magnetic frustration, isotropic HOIs, and DMI.

II. CALCULATION METHOD

First-principles calculations are carried out based on density functional theory (DFT) implemented in the Vienna
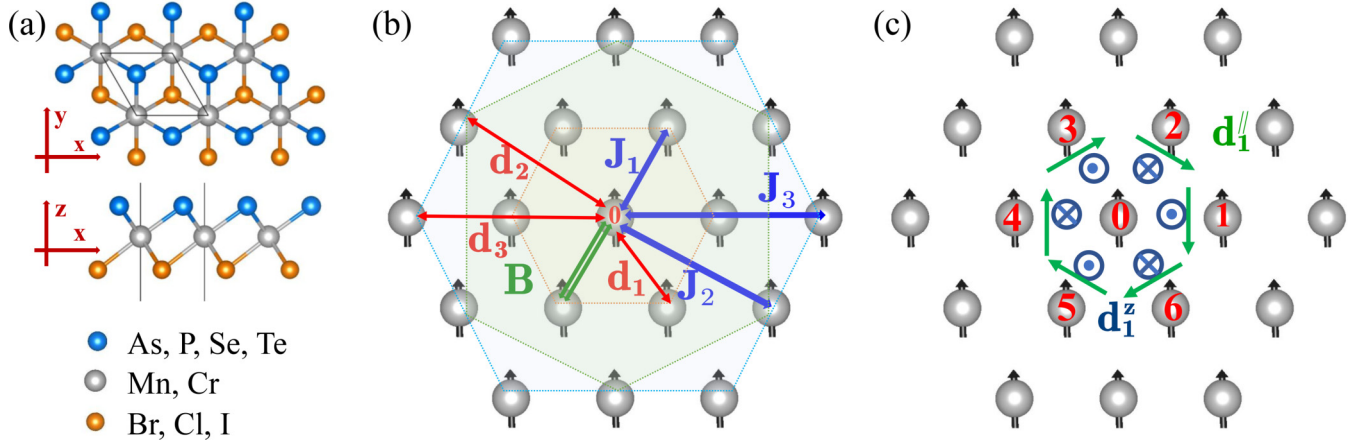
*hongxin.yang@nju.edu.cn

054408-1

FIG. 1. (a) Top and side views of the crystal structures of MnXZ and CrYZ (X = P, As; Y = Se, Te; and Z = Cl, Br, I) monolayers. (b) Schematic representation of DMI and Heisenberg exchange interactions up to third neighbor and nearest-neighbor biquadratic interactions. (c) Diagrammatic sketch of the six nearest-neighbor DMI components $d_1^{\parallel}$ and d_1^z between atomic sites 1, 2, 3, 4, 5, 6, and 0.

Ab initio Simulation Package [54–56]. The electron-ion interaction is described by the projected augmented-wave method, and the electronic exchange-correlation functional is treated by the generalized gradient approximation (GGA) of the Perdew-Burke-Ernzerhof form [57,58]. We employ the GGA+U method with effective $U_{\mathrm{eff}} = 3\,\mathrm{eV}$ to describe the strongly correlated $3d$ orbitals of Cr and Mn atoms. The plane-wave cutoff energy is set to 500 eV, and the first Brillouin zone is sampled by Γ-centered $24 \times 24 \times 1$ k-point meshes. We set the vacuum layer with a thickness of 15 Å to eliminate interactions between the periodic images. The convergence criterion of electronic iteration is set to 10^{-7} eV. All our structure relaxations are performed until the Hellmann-Feyman forces are <0.001 eV/ Å. The phonon spectra of the MnXZ monolayers are calculated with $4 \times 4 \times 1$ supercells, by using the PHONOPY code [59].

III. RESULTS AND DISCUSSIONS

Top and side views of the crystal structures of the Janus MnXZ and CrYZ (X = P, As; Y = Se,Te; and Z = Cl, Br, I) monolayers are presented in Fig. 1(a). To confirm the structural stability of the MnXZ monolayers, we calculate phonon spectra in Fig. S1 in the Supplemental Material [60]. The calculated in-plane lattice parameters and saturation magnetization of MnXZ and CrYZ are shown in Table I. For these monolayers, we adopt the following spin model Hamiltonian to describe the interactions between the Mn and Cr atoms:

$$H = -\frac{1}{2}\sum_{i,j} J_{ij}(\mathbf{S}_i \cdot \mathbf{S}_j) - \frac{1}{2}\sum_{i,j} \mathbf{d}_{ij} \cdot (\mathbf{S}_i \times \mathbf{S}_j)$$
$$- K_{\mathrm{MCA}} \sum_i \left(\mathbf{S}_i^z\right)^2 + E_{\mathrm{ddi}} + H_{\mathrm{HOI}}, \tag{1}$$

where

$$H_{\mathrm{HOI}} = -\frac{1}{2}B_1 \sum_{<i,j>} (\mathbf{S}_i \cdot \mathbf{S}_j)^2$$
$$- Y_1 \sum_{i,j,k}[(\mathbf{S}_i \cdot \mathbf{S}_j)(\mathbf{S}_j \cdot \mathbf{S}_k) + (\mathbf{S}_j \cdot \mathbf{S}_k)(\mathbf{S}_k \cdot \mathbf{S}_i)$$

$$+ (\mathbf{S}_i \cdot \mathbf{S}_k)(\mathbf{S}_i \cdot \mathbf{S}_j)]$$
$$- \frac{1}{4}F_1 \sum_{i,j,k,l}[(\mathbf{S}_i \cdot \mathbf{S}_j)(\mathbf{S}_k \cdot \mathbf{S}_l) + (\mathbf{S}_i \cdot \mathbf{S}_l)(\mathbf{S}_j \cdot \mathbf{S}_k)$$
$$- (\mathbf{S}_i \cdot \mathbf{S}_k)(\mathbf{S}_j \cdot \mathbf{S}_l)]. \tag{2}$$

In Eqs. (1) and (2), $\mathbf{S}_i$ and $\mathbf{S}_j$ are the spin unit vector of each atom at sites i and j. Also, J_{ij} and $\mathbf{d}_{ij}$ denote the Heisenberg exchanges and DMI interactions. Further, H_{HOI} represents the isotropic higher-order Hamiltonian, including two-site-four-spin interaction, or biquadratic interaction B_1, three-sites-four-spin interaction Y_1, and four-sites-four-spin interaction F_1. Noncentrosymmetric systems could also exhibit chiral four-spin interactions [61–66]. The magnitude of such terms could be significant in lower-dimensional systems such as magnetic adatoms [61,64] or one-dimensional magnetic atom chains [63], but it is much weaker in ferromagnetic monolayers [65]. Thus, we neglect the chiral multispin interactions in the Hamiltonian.

As shown in Fig. 1(b), we consider the Heisenberg exchanges and DMI interactions up to the third neighbor, namely, the NN interactions J_1 and $\mathbf{d}_1$, the next-NN (NNN) interactions J_2 and $\mathbf{d}_2$, and the NNNN interactions J_3 and $\mathbf{d}_3$. The symmetry of the MnXZ and CrYZ Janus monolayers is C_{3v}, in which the Bloch-type DMI vanishes according to the Moriya rules [9]. The nonvanishing DMI components between each NN, NNN, and NNNN Mn (Cr) pair are the Néel type, which can be expressed as $\mathbf{d}_{ij} = d^{\parallel}(\hat{r}_{ij} \times \hat{z}) + d^z\hat{z}$, where d^z and $d^{\parallel}$ represent the perpendicular and in-plane components of DMI, respectively. Also, $\hat{r}_{ij}$ represents a unit vector pointing from i to j, and $\hat{z}$ is normal to the plane. Previous works proved that the d_z components change their sign for the six neighboring pairs. As a representative example, Fig. 1(a) shows the directions of d_1^z for the six NN pairs of Mn (Cr) atoms. Here, K_{MCA} indicates magnetocrystalline anisotropy energy (MAE), which is calculated by comparing the energy difference between self-consistent energies, while the magnetic axis aligns along (100) and (001) orientations. The calculated values of magnetic anisotropy of all MnXZ and CrYZ monolayers are shown in Table I. Here,

TABLE I. The calculated lattice constant a, saturation magnetization M_s, in-plane and out-of-plane DMI components up to NNNN, magnetocrystalline anisotropy K_{MCA} for the MnXZ and CrYZ (X = P, As; Y = Se, Te; and Z = Cl, Br, I) monolayers. DMI values and K_{MCA} are in meV.

Structure	a (Å)	M_s (μB)	$d_1^{//}$	$d_2^{//}$	$d_3^{//}$	d_1^z	d_2^z	d_3^z	K_{MCA}
MnAsBr	3.645	3.507	−5.65	0.19	−1.02	0.52	−0.06	0.33	1.29
MnAsI	3.895	3.436	−5.54	0.33	0.17	−0.36	−0.07	0.58	1.04
MnPBr	3.589	3.376	−2.14	0.92	0.30	−0.19	−0.01	0.13	0.11
MnPCl	3.452	3.344	−1.75	0.07	−0.02	0.26	−0.01	0.09	0.05
CrSeCl	3.592	2.971	−1.11	0.01	−0.23	0.24	−0.01	0.16	−0.11
CrSeBr	3.681	2.977	−1.53	0.03	−0.17	0.26	−0.01	0.09	−0.24
CrSeI	3.835	2.989	−2.34	0.06	−0.04	0.36	−0.03	0.07	0.27
CrTeCl	3.763	3.045	−2.19	0.06	−1.13	0.66	0.04	0.82	−2.27
CrTeBr	3.850	3.049	−2.81	0.09	−1.01	0.68	−0.03	0.75	−2.83
CrTeI	3.995	3.057	−4.08	0.18	−0.82	0.79	−0.02	0.64	−1.01

E_{ddi} is the dipole-dipole energy, which is included in all our atomistic spin model simulations.

A. The DMI components

We implement the qSO method [21,67,68] to determine both the in-plane and perpendicular DMI components for the MnXZ and CrYZ monolayers. The qSO method is based on first-order perturbation theory [69] of the generalized Bloch theorem (gBT) [70]. By constraining the SOC Hamiltonian to a single component along the spin-spiral rotation axis, the qSO method allows us to calculate the SOC-included spin-spiral Hamiltonian in self-consistent DFT calculations. Here, we introduce two different flat Néel-type spin spirals propagating along the high-symmetry direction Γ-K of reciprocal space, namely, the out-of-plane spiral within the spins rotating in the x-z plane and the in-plane spiral within the spins rotating in the x-y plane, as plotted in Figs. 2(a) and 2(b). The magnetic moment at an atom site R_i in the former spin spiral is described as $M_i = M[\sin(q \cdot r_i), 0, \cos(q \cdot r_i)]$ and for the latter $M_i = M[\sin(q \cdot r_i), \cos(q \cdot r_i), 0]$.

As a representative example, we plot the out-of-plane and in-plane spirals for the MnAsBr monolayer in Figs. 2(c) and 2(d). The black triangles in Figs. 2(c) and 2(d) represent the non-SOC spin-spiral energy dispersion from gBT. Here, the non-SOC spin-spiral dispersion for the out-of-plane and in-plane spirals in Figs. 2(c) and 2(d) are degenerate. The energy minima of the non-SOC $E[q]$ locates at around $q = \pm 0.1(\frac{2\pi}{a})$ due to the competing NN ferromagnetic and beyond-NN antiferromagnetic exchanges, which we will discuss later. As plotted by the red dots in Fig. 2(c), when SOC is included, the out-of-plane spin-spiral energy $E[q]$ favors clockwise (cw) rotation and shows strongly asymmetric behavior around the ferromagnetic state of $q = 0$, indicating the existence of strong in-plane DMI with cw chirality. Interestingly, the impact of SOC on the energy dispersion for the in-plane spin spiral is much weaker, as shown in Fig. 2(d). In the regions of $0.3 (\frac{2\pi}{a}) \leqslant |q| \leqslant 0.7(\frac{2\pi}{a})$, the SOC-included in-plane spin-spiral energy $E[q]$ slightly deviates from the non-SOC spin spiral and favors anticlockwise (acw) rotation.

The respective DMI energy is derived by $\Delta E_{DM}[q] = (E[q] - E[-q])/2$. In Fig. 2(e), $\Delta E_{DM}^{//}[q]$ shows a sinusoidal behavior and is linearly dependent on q in the the interval be-

tween $q = \pm 0.1(\frac{2\pi}{a})$. The overall in-plane DMI of MnAsBr shows a cw chirality. Other MnXZ and CrYZ monolayers also show cw in-plane DMI, as shown in Fig. S2 in the Supplemental Material [60]. The slope of $\Delta E_{DM}^z[q]$ is infinitesimal in the interval between $q = \pm 0.05(\frac{2\pi}{a})$, as shown in Figs. 2(f) and S3 in the Supplemental Material [60]. Here, $\Delta E_{DM}^z[q]$ is significant around the neighborhoods of $q = \pm 0.5(\frac{2\pi}{a})$, indicating that the d_z components are short-range effects [17,22].

For a Mn (Cr) atom at site 0, the total DMI energy can be described as the sum of each NN, NNN, and NNNN pair [71]:

$$E_{DM} = \frac{1}{2}\sum_{<i>} \mathbf{d}_{0i} \cdot (\mathbf{S}_0 \times \mathbf{S}_i) + \frac{1}{2}\sum_{<<i>>} \mathbf{d}_{0i} \cdot (\mathbf{S}_0 \times \mathbf{S}_i)$$
$$+ \frac{1}{2}\sum_{<<<i>>>} \boldsymbol{d}_{0i} \cdot (\mathbf{S}_0 \times \mathbf{S}_i). \quad (3)$$

For the MnXZ and CrYZ monolayers, the total DMI energy consists of the contributions from in-plane and out-of-plane components: $E_{DM} = \Delta E_{DM}^{//}[q] + \Delta E_{DM}^z[q]$. For a Mn (Cr) atom at site 0, $\Delta E_{DM}^{//}[q]$ and $\Delta E_{DM}^z[q]$ can be expressed as the sum of each NN, NNN, and NNNN pair:

$$\Delta E_{DM}^{//}[q] = \sum_{<i>} d_{0i}^y \cdot \sin(\mathbf{q} \cdot \mathbf{r}_{0i}) + \sum_{<<i>>} d_{0i}^y \cdot \sin(\mathbf{q} \cdot \mathbf{r}_{0i})$$
$$+ \sum_{<<<i>>>} d_{0i}^y \cdot \sin(\mathbf{q} \cdot \mathbf{r}_{0i}), \quad (4)$$

$$\Delta E_{DM}^z[q] = \sum_{<i>} d_{0i}^z \cdot \sin(\mathbf{q} \cdot \mathbf{r}_{0i}) + \sum_{<<i>>} d_{0i}^z \cdot \sin(\mathbf{q} \cdot \mathbf{r}_{0i})$$
$$+ \sum_{<<<i>>>} d_{0i}^z \cdot \sin(\mathbf{q} \cdot \mathbf{r}_{0i}), \quad (5)$$

where $\mathbf{r}_{0i}$ denotes the vectors pointing from atomic site 0 to i [$i = 1, 2, 3, 4, 5,$ and 6, see Fig. 1(c)]. In Eqs. (4) and (5), the $\mathbf{q}$ vectors represent x-z and x-y spirals, respectively. We note that, for the $d^{//}$ components, only the d^y components from each pair contribute to $\Delta E_{DM}^{//}[q]$. For d^z components, the sign of d^z changes in a staggered way. For a hexagonal lattice with the $\mathbf{q}$ vector propagating along the Γ-K direction of the reciprocal space, we can sum up the analytical forms of
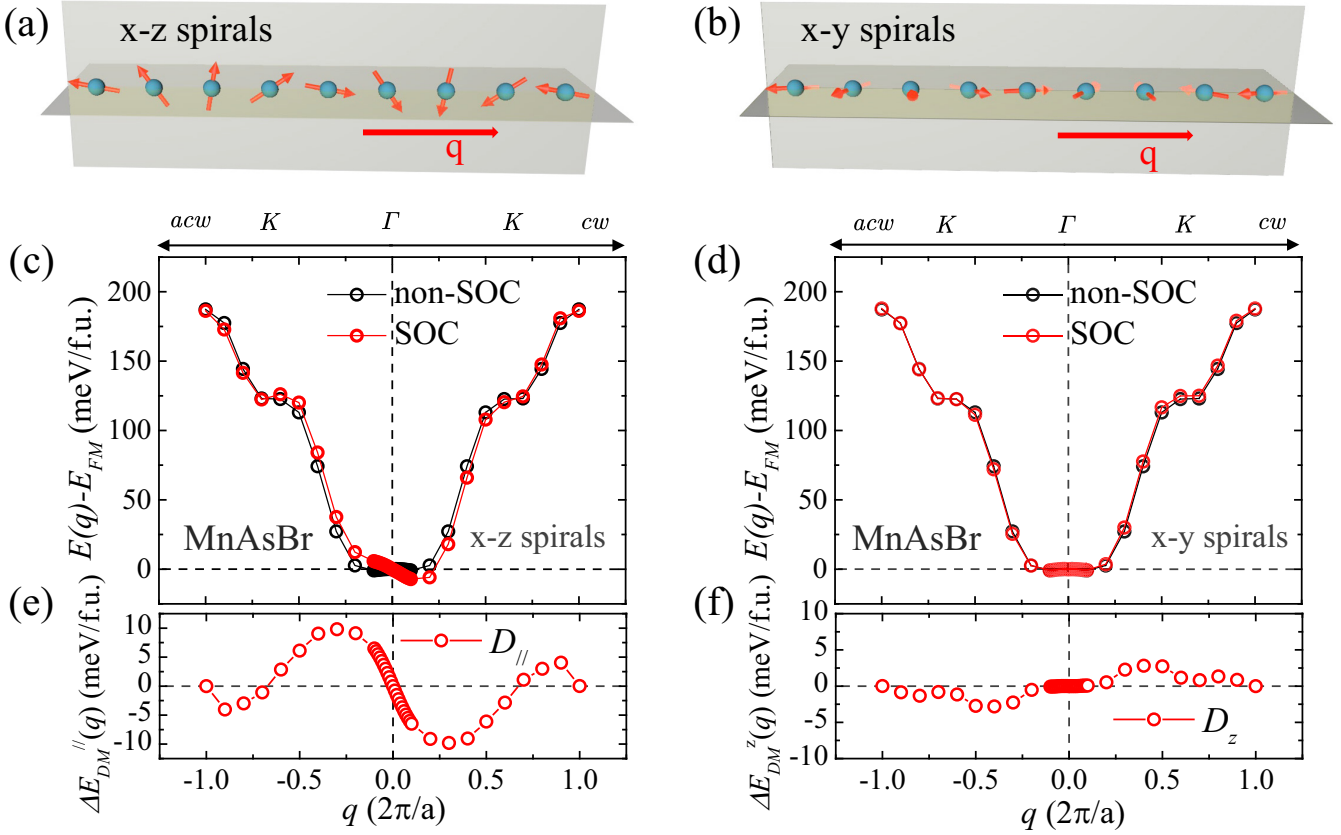
FIG. 2. Schematics of spin spirals in the (a) *x-z* plane and (b) *x-y* plane. (c) and (d) Calculated spin-spiral energy $E[q]$, and (e) and (f) DMI energy $\Delta E_{DM}[q]$ as functions of spiral vector length q along the Γ-K direction of the reciprocal space. $E[q]$ is given with respect to the ferromagnetic state at $q = 0$. (c) and (e) are plotted for the spirals in the *x-z* plane, in which red and black circles are calculated with spin-orbit coupling (SOC) and without SOC (non-SOC), respectively. (d) and (f) are plotted for the spirals in the *x-y* plane, in which red and black circles are obtained with and without SOC, respectively.

energy contributions from six NN, six NNN, and six NNNN pairs as follows:

$$\Delta E_{DM}^{//}[q] = [2\sin(2\pi q) + 2\sin(\pi q)]d_1^{//}$$
$$+ [2\sqrt{3}\sin(3\pi q)]d_2^{//}$$
$$+ [2\sin(4\pi q) + 2\sin(2\pi q)]d_3^{//}, \quad (6)$$

$$\Delta E_{DM}^z[q] = [2\sin(\pi q) - 4\sin(2\pi q)]d_1^z + [4\sin(3\pi q)]d_2^z$$
$$+ [2\sin(2\pi q) - 4\sin(4\pi q)]d_3^z, \quad (7)$$

where q denotes the spiral length. By substituting the values of $E_{DM}^{//}[q]$ in Fig. 2(e) and the lower panels of Figs. S2(a)–S2(i) in the Supplemental Material [60] into Eq. (6), we can determine the $d^{//}$ components for the MnXZ and CrYZ monolayers from multiple linear regression. Similarly, through substituting the values of $E_{DM}^z[q]$ in Fig. 2(f) and the lower panels of Fig. S3(a)–S3(i) in the Supplemental Material [60] into Eq. (7), we can fit the d^z values for MnXZ and CrYZ monolayers. The calculated results are listed in lines 4–9 of Table I. The $d_1^{//}$ components are the largest for each MnXZ and CrYZ monolayer, while the d_1^z components are about one order smaller than $d_1^{//}$. The NNN DMI $d_2^{//}$ and d_2^z are the smallest for most of the MnXZ and CrYZ monolayers.

The contribution from NNNN DMI $d_3^{//}$ and d_3^z are significant in MnAsBr, CrTeCl, CrTeBr, and CrTeI.

To elucidate the microscopic origin of DMI in the MnXZ and CrYZ monolayers, we plot the atomic-layer-resolved SOC energies associated with in-plane and out-of-plane DMI at $q = 0.2(\frac{2\pi}{a})$ in Figs. 3(a) and 3(b). From Fig. 3(a), it is found that the in-plane DMI energy is mainly contributed by the P, As, or chalcogen atoms, and contributions from the halogen atoms are very weak. We choose CrTeI and MnAsI monolayers as representative examples to show the atomic DMI energy contributions for spin spirals rotating in both *x-z* and *x-y* planes, respectively. As shown in Figs. 3(c) and 3(e), the dominant contributions of in-plane DMI come from Te and As atoms for CrTeI and MnAsI monolayers, respectively. Interestingly, in the larger-q region, the contribution from I atoms becomes significant in both CrTeI and MnAsI monolayers in Figs. 3(d) and 3(f).

The contribution from I atoms in MnAsI overcomes that from As atoms while $|q| > 0.4$ $(\frac{2\pi}{a})$, indicating that larger contributions of SOC energy to shorter-range d^z can be found in I atoms, whereas the As atoms contribute more SOC energy to longer-range d^z. Because the out-of-plane DMI contributions from As and I atoms have opposite chirality due to symmetric reasons, the signs of d_1^z and d_3^z are opposite.
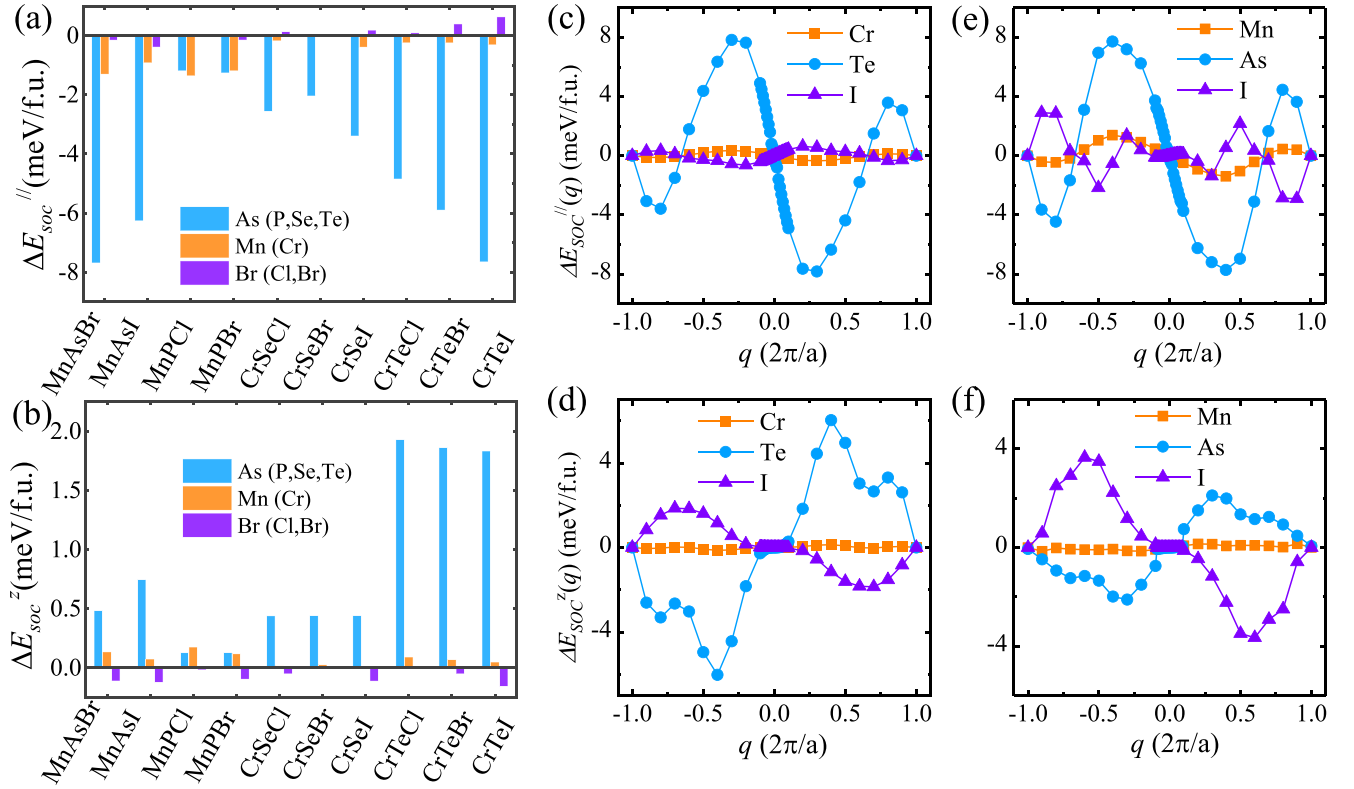
FIG. 3. Selective atomic-layer-resolved spin-orbit coupling (SOC) energy of the (a) in-plane DMI and (b) out-of-plane DMI at $q = 0.2(\frac{2\pi}{a})$ for all the MnXZ and CrYZ monolayers, respectively. Atomic-layer-resolved SOC energy of (c) and (e) in-plane DMI and (d) and (f) out-of-plane DMI plotted for CrTeI and MnAsI monolayers, respectively.

B. Heisenberg exchanges and HOIs

The spin-spiral energy dispersion $E_{SS}[q]$ is governed by NN, NNN, and NNNN Heisenberg exchanges, the two-site biquadratic interaction B_{ij}, and three-site interaction Y_{ijk} [22,40,48,72]. The four-site interaction F_{ijkl} does not contribute to $E_{SS}[q]$. Figure 4(a) shows the schematic representation of the HOIs B_{ij}, Y_{ijk}, and F_{ijkl}, which originate from multiple electrons hoping among two or more magnetic atomic sites [40]. For a spin spiral propagating along the Γ-K direction, the relation between $E_{SS}[q]$ and the Heisenberg exchanges up to the NNNN and HOIs B_{ij} and Y_{ijk} is described
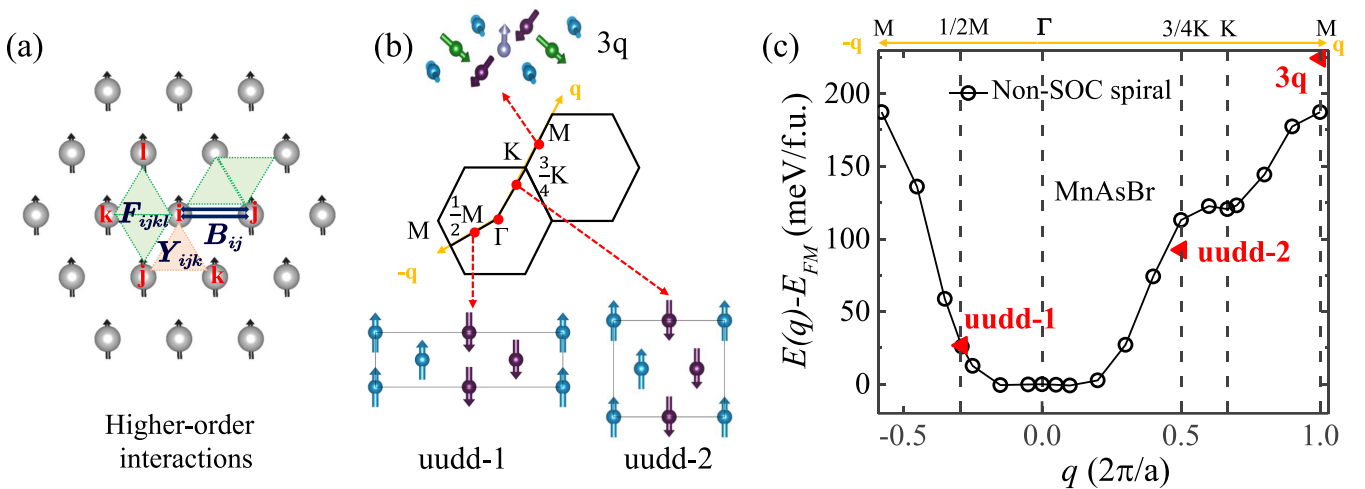

FIG. 4. (a) Diagrammatic sketch of the higher-order interactions. (b) Schematics of the magnetic configurations of up-up-down-down-1 (uudd-1), up-up-down-down-2 (uudd-2), 3q states, and the spiral-propagating directions in the reciprocal space. (c) The black circles represent the energy dispersion for the spin spiral without spin-orbit coupling (SOC) in the x-y plane for MnAsBr, where the spin-spiral vector length q is along the Γ-M and Γ-K directions. $E[q]$ is given with respect to the ferromagnetic state at $q = 0$. The red triangles indicate the relative energy per unit cell for the uudd-1, uudd-2, and 3q states, respectively.

as follows [22,72]:

$$
\begin{aligned}
E_{SS}[q] = &-[\cos(2\pi q) + 2\cos(\pi q)](J_1 + 2Y_1) \\
&- [1 + 2\cos(3\pi q)](J_2 + 2Y_1) \\
&- [\cos(4\pi q) + 2\cos(2\pi q)](J_3 + B_1).
\end{aligned} \tag{8}
$$

For the non-SOC spirals in Figs. 2(e) and S2(a)–S2(i) in the Supplemental Material [60], we can fit the terms $J_1 + 2Y_1$, $J_2 + 2Y_1$, and $J_3 + B_1$ by multiple linear regression. Next, we calculate the respective HOIs.

To determine the HOIs B_1, Y, and F, we need to compare the non-SOC relative energy between three pairs of magnetic configurations [72]. The first pair consists of a so-called up-up-down-down-1 (uudd-1) antiferromagnetic state [see Fig. 4(b)] and the spin-spiral state at $\frac{1}{2}(\Gamma-M)$ [abbreviated as $\frac{1}{2}M$ in Fig. 4(c)]. The second pair includes an up-up-down-down-2 (uudd-2) state [see Fig. 4(b)] and the spin-spiral state at $\frac{3}{4}(\Gamma-K)$ [abbreviated as $\frac{3}{4}K$ in Fig. 4(c)]. The third pair contains a noncollinear magnetic configuration known as the $3q$ state [73], and the spin-spiral state at the M point, which is known as the Néel antiferromagnetic state. The spin-spiral states at $\frac{1}{2}(\Gamma-M)$ and $\frac{3}{4}(\Gamma-K)$ are two 90° spirals. Here, Γ-centered k-points of $14 \times 44 \times 1$, $22 \times 28 \times 1$, and $15 \times 15 \times 1$ are used for calculating the relative energy of the uudd-1, uudd-2, and $3q$ states, respectively [72]. The relative energy of the uudd-1, uudd-2, and $3q$ states are expressed as $E_{uudd/3q} = \frac{1}{4}(E_{uudd/3q}^{AFM} - E_{uudd/3q}^{FM})$, where $E_{uudd/3q}^{FM}$ is the energy of FM states for the respective supercells in Fig. 4(b).

As a representative example in Fig. 4(c), we plot the non-SOC spin-spiral energy $E[q]$ for MnAsBr. The red triangles in Fig. 4(c) denote the relative energy per atom E_{uudd-1}, E_{uudd-2}, and E_{3q}, respectively. We can solve the values of HOIs from the following equations [72]:

$$
E_{uudd-1} - E_{\frac{1}{2}M} = \frac{16}{3}(2F_1 + B_1 - Y_1), \tag{9}
$$

$$
E_{uudd-2} - E_{\frac{3}{4}K} = 4(2F_1 - B_1 - Y_1), \tag{10}
$$

$$
E_{3q} - E_M = 4(2F_1 - B_1 + Y_1). \tag{11}
$$

From Figs. 4(c) and S4(a)–S4(c) in the Supplemental Material [60], we obtain the HOI parameters for all the MnXZ and CrYZ monolayers. By subtracting B_1 and Y_1 from the aforementioned terms $J_1 + 2Y_1$, $J_2 + 2Y_1$ and $J_3 + B_1$, we solve the NN, NNN and NNNN Heisenberg exchanges for the MnXZ and CrYZ monolayers. The calculated J_1, J_2 and J_3 and HOIs are shown in Table II. From Table II, MnXZ and CrYZ monolayers exhibit strong ferromagnetic NN exchange J_1. The NNN ferromagnetic exchange J_2 for the MnXZ and CrYZ monolayers are much weaker compared to J_1. Interestingly, the values of NNNN exchange interaction J_3 of MnXZ and CrYZ monolayers are negative, indicating competing antiferromagnetic exchange.

The values of biquadratic interaction B_1 range from 3.38 to 4.02 meV for MnXZ and from 2.12 to 2.86 meV for CrYZ, which are the same order compared with biquadratic interactions of previous studies, such as LiCrTe$_2$ [22], CrSiTe$_3$ [48], and CrGeTe$_3$ [48]. The values of three-site interaction Y_1 are comparable with B_1 for Mn-based monolayers. For Cr-based systems, Y_1 magnitudes are much weaker.

TABLE II. The NN, NNN, NNNN Heisenberg exchange J_1, J_2 and J_3, the biquadratic interaction B_1, three-site interaction Y_1, and four-site interaction F_1 for the MnXZ and CrYZ ($X = $ P, As; $Y = $ Se,Te; and $Z = $ Cl, Br, I) monolayers. All parameters are in meV.

Structure	J_1	J_2	J_3	B_1	Y_1	F_1
MnAsBr	50.08	8.13	−20.88	3.38	−2.67	0.45
MnAsI	85.37	4.43	−11.37	3.97	−3.74	1.25
MnPBr	80.01	7.09	−13.65	4.02	−3.48	0.72
MnPCl	65.02	8.74	−17.31	3.39	−3.13	0.14
CrSeCl	22.53	0.36	−4.25	2.12	0.06	0.96
CrSeBr	24.73	0.31	−3.69	2.15	0.08	1.04
CrSeI	25.40	0.18	−3.15	2.26	0.14	1.10
CrTeCl	16.49	1.48	−11.40	2.66	−0.38	0.55
CrTeBr	21.44	1.32	−9.71	2.71	−0.32	0.76
CrTeI	26.61	1.13	−7.60	2.86	−0.22	0.98

Since both NNNN frustration and DMI can induce topological spin textures, we calculate the frustration ratios $|J_3|/J_1$ and DMI ratios $|d_1^{//}|/J_1$ for all the MnXZ and CrYZ monolayers. MnAsBr, CrTeBr, and CrTeCl monolayers have the largest frustration ratios $|J_3|/J_1$ of 0.42, 0.45, and 0.69, respectively, which are noted as strong frustration in Fig. 5. Interestingly, for these three monolayers, the NNNN DMI $d_3^{//}$ and d_3^z are more significant than that of other monolayers, as shown in Table I. The frustration ratios $|J_3|/J_1$ of CrTeI and MnPCl monolayers are 0.29 and 0.27, respectively, which are labeled as medium frustration in Fig. 5. The frustration ratios for CrTeI and MnPCl are larger than the critical value to exhibit frustration-induced skyrmionic spin textures of $|J_3|/J_1 = 0.25$ [33]. However, the non-SOC ground states of CrTeI and MnPCl are ferromagnetic due to the presence of biquadratic interaction B_1, which agrees with the results in previous studies [22,48]. For the other monolayers, namely, MnAsI, MnPBr, CrSeBr, and CrSeCl, the frustration ratios are <0.25, which are noted as weak frustration in Fig. 5.

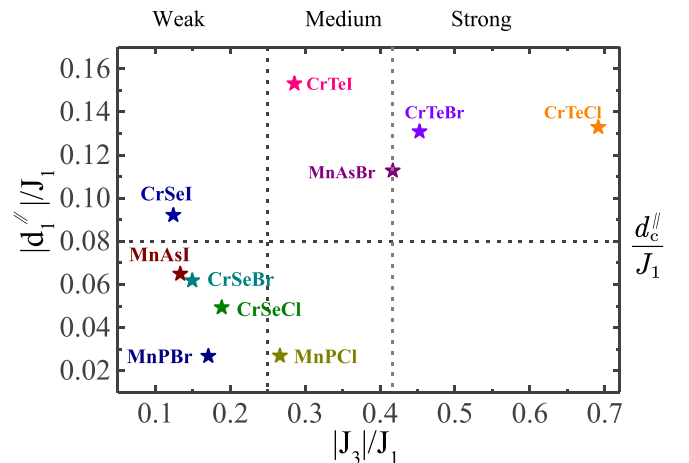We adopt the critical DMI ratio of $|d_c^{//}|/J_1 = 0.08$ [1,17,22] to describe whether topological magnetism could

FIG. 5. The ratios of $|d_1^{\parallel}|/J_1$ and $|J_3|/J_1$ for all the MnXZ ($X = $ P, As; and $Z = $ Cl, Br, I) and CrYZ ($T = $ Se, Te; and $Z = $ Cl, Br, I) monolayers.
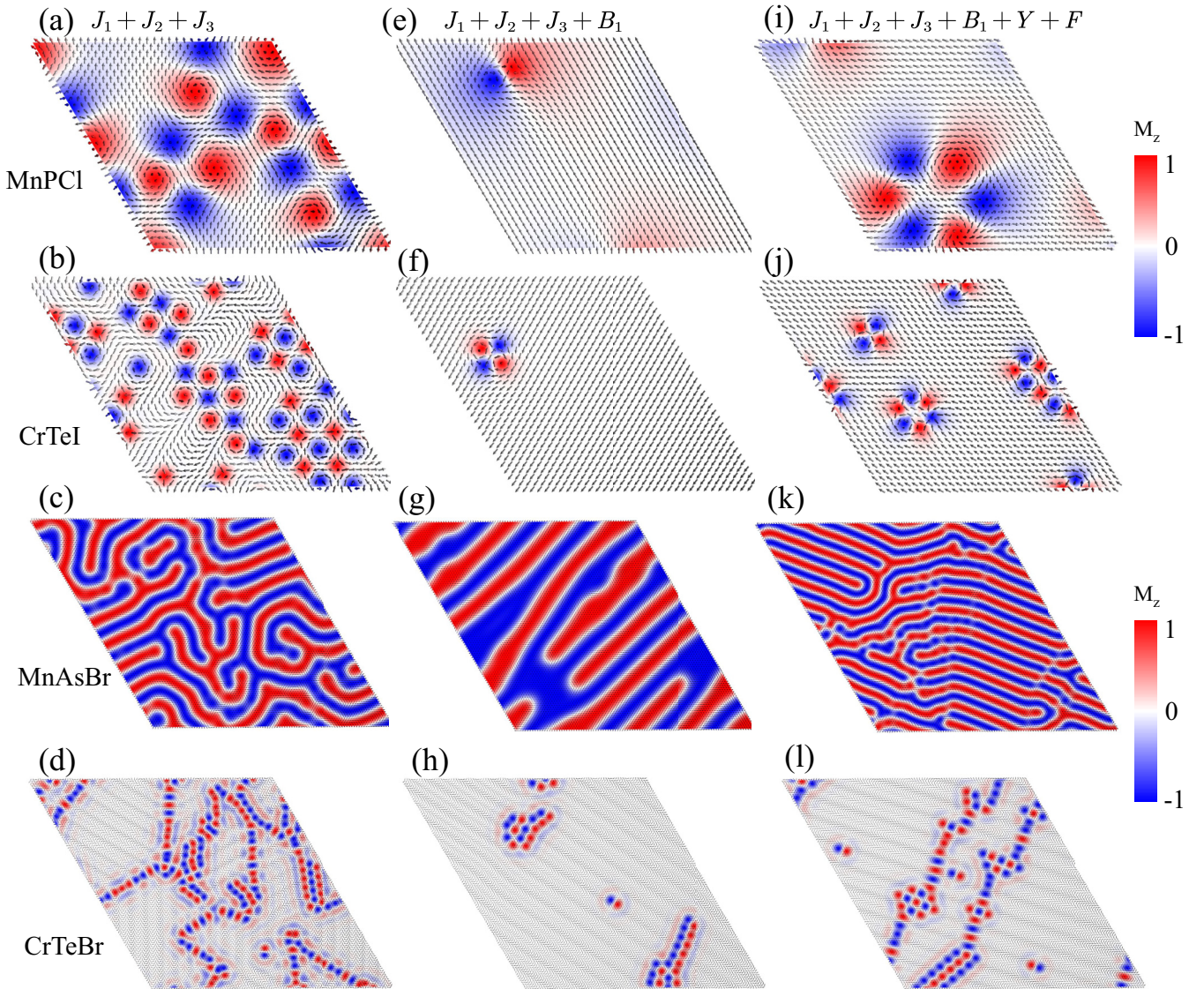
FIG. 6. The relaxed magnetization configurations in a periodical nanodisk with 100×100 atoms in the absence of external field for (a) MnPCl, (b) CrTeI, (c) MnAsBr, and (d) CrTeBr monolayers, in which we neglect the DMI vectors and all the higher-order interactions (HOIs) of Eq. (1). The relaxed magnetization configurations without external field in a periodical nanodisk with 100×100 atoms for (e) MnPCl, (f) CrTeI, (g) MnAsBr, and (h) CrTeBr monolayers, in which we consider the interplay between Heisenberg exchanges and biquadratic interactions. The relaxed magnetization configurations without external field in a periodical nanodisk with 100×100 atoms for (i) MnPCl, (j) CrTeI, (k) MnAsBr, and (l) CrTeBr monolayers, in which we consider the interplay between Heisenberg exchanges and the isotropic HOIs. The color map indicates the out-of-plane spin components of Mn and Cr atoms.

be formed by DMI in a magnet. Judging from the critical DMI ratios, we classified MnXZ and CrYZ monolayers into two categories. Category I consists of CrSeI, CrTeI, MnAsBr, CrTeBr, and CrTeCl monolayers, with an increasing trend of frustration ratios. The DMI ratios of the monolayers in category I are beyond the critical value of 0.08. On the contrary, category II contains the monolayers MnAsI, CrSeBr, MnPBr, CrSeCl, and MnPCl; each shows a DMI ratio below the critical value.

C. Atomistic spin model simulations

With all the magnetic parameters obtained in Tables I and II, we perform the atomistic spin model simulations with

the SPIRIT code [74]. The spin evolution is described by the Landau-Lifshitz-Gilbert (LLG) equation, which reads

$$\frac{\partial \mathbf{S}_i}{\partial t} = -\frac{\gamma}{1 + \alpha^2} \left\{ \mathbf{S}_i \times \mathbf{B}_{\text{eff}}^i + \left[\alpha \mathbf{S}_i \times \left(\mathbf{S}_i \times \mathbf{B}_{\text{eff}}^i \right) \right] \right\}, \quad (12)$$

in which γ and α denote the gyromagnetic ratio and damping constant, respectively. Also, $\mathbf{S}_i$ is the unit vector of spin moment of site i, and $\mathbf{B}_{\text{eff}}^i$ is the on-site effective magnetic field, which is described as $\mathbf{B}_{\text{eff}}^i = -\frac{1}{\mu_s} \frac{\partial H}{\partial \mathbf{S}_i}$, where H is the spin Hamiltonian for the MnXZ and CrYZ monolayers. For atomistic simulation with SPIRIT code, a $100 \times 100 \times 1$ periodical supercell is adopted, and the number of iteration steps is set to 2×10^5 to reach the stable configurations. For comparison, we perform the atomistic simulation by using the VAMPIRE code
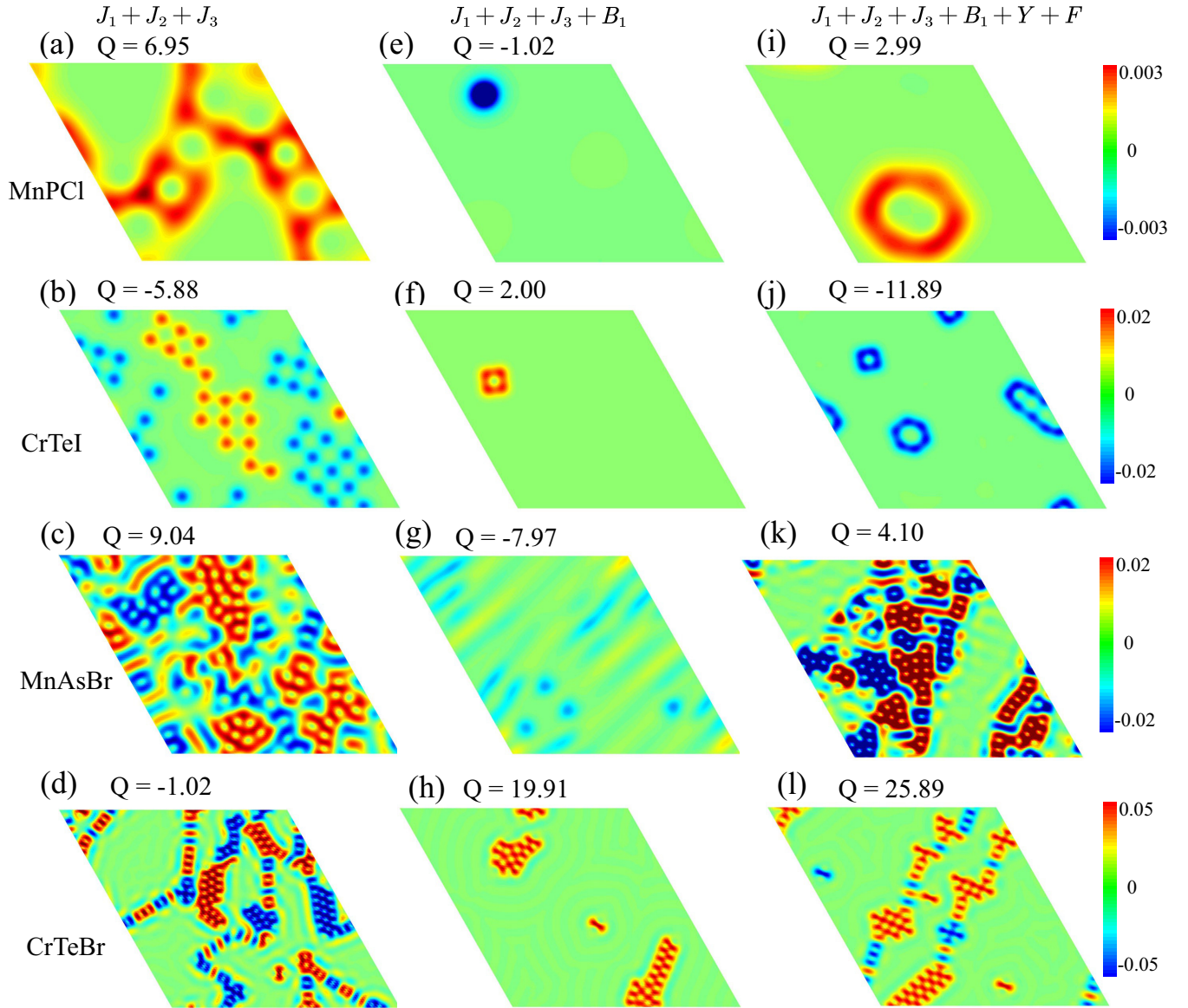
FIG. 7. The distribution of topological charge in a periodical nanodisk with 100×100 atoms in the absence of external field for (a) MnPCl, (b) CrTeI, (c) MnAsBr, and (d) CrTeBr monolayers, in which we neglect the DMI vectors and all the higher-order interactions (HOIs) of Eq. (1). The distribution of topological charge in a periodical nanodisk with 100×100 atoms in the absence of external field for (e) MnPCl, (f) CrTeI, (g) MnAsBr, and (h) CrTeBr monolayers, in which we consider the interplay between Heisenberg exchanges and biquadratic interactions. The distribution of topological charge in a periodical nanodisk with 100×100 atoms in the absence of external field for (i) MnPCl, (j) CrTeI, (k) MnAsBr, and (l) CrTeBr monolayers, in which we consider the interplay between Heisenberg exchanges and the isotropic HOIs. Red (blue) in the color bars indicate positive (negative) topological charge densities, while green denotes zero topological charge density.

[75], with the same LLG-Heun method, which are shown in the Supplemental Material [60]. We use $\alpha = 0.2$ for all the spin dynamics.

1. Interplay between frustration and HOI terms

For the monolayers with sizable magnetic frustration, field-free topological magnetism can emerge even without the presence of DMI. Thus, we adopt a Hamiltonian of $H = -\frac{1}{2}\sum_{i,j} J_{ij}(\mathbf{S}_i \cdot \mathbf{S}_j) - K_{\mathrm{MCA}}\sum_i (\mathbf{S}_i^z)^2 + E_{\mathrm{ddi}}$ to examine the frustration-induced topological magnetism in MnPCl, CrTeI, MnAsBr, and CrTeBr.

We note that the frustration ratio $|J_3|/J_1$ increases while evolving MnPCl, CrTeI, MnAsBr, and CrTeBr. Figure 6(a) shows that meron-like vortex pairs [32] can be found in MnPCl, which exhibit moderate frustration ratio and infinitesimal PMA. For CrTeI in Fig. 6(b) with in-plane MAE (IMA) of -1.01 meV/f.u., randomly distributed Bloch-type skyrmions, Bloch-type bimerons, and antiskyrmions are found, which is consistent with previous results [39]. For MnAsBr with perpendicular MAE (PMA) of 1.29 meV/f.u., the ground magnetic state is the so-called Bloch line configuration [50,76,77], as plotted in Fig. 6(c). Figure 6(d) shows that bimeron chains with randomly distributed helicities can be
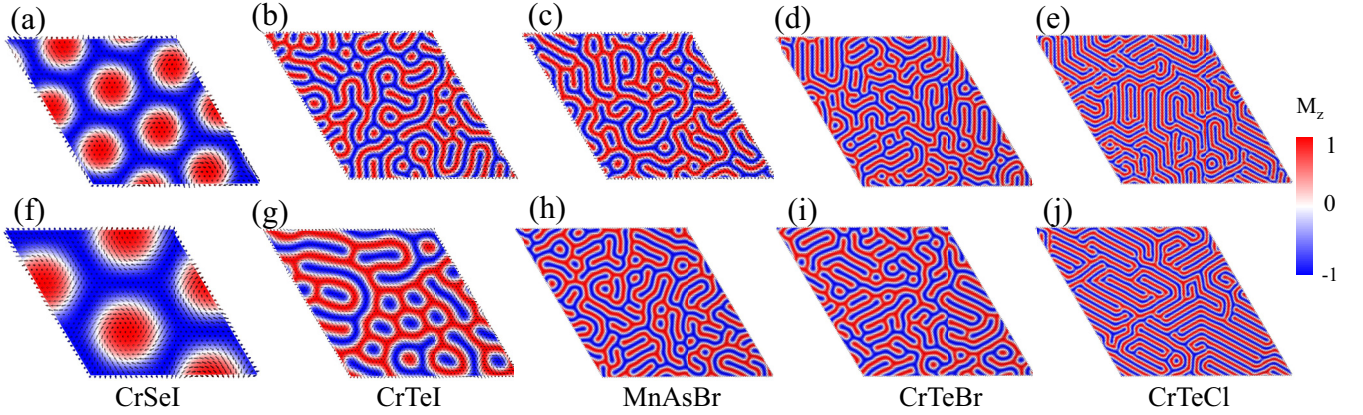
FIG. 8. The relaxed magnetization configuration in a periodical nanodisk with 100×100 atoms in the absence of external field for (a) CrSeI, (b) CrTeI, (c) MnAsBr, (d) CrTeBr, and (e) CrTeCl, in which we neglect the higher-order interaction (HOI) terms of the Hamiltonian in Eq. (1). The relaxed magnetization configuration in a periodical nanodisk with 100×100 atoms in the absence of external field for (f) CrSeI, (g) CrTeI, (h) MnAsBr, (i) CrTeBr, and (j) CrTeCl with the Hamiltonian in Eq. (1). The color map indicates the out-of-plane spin components of Mn and Cr atoms.

stabilized in the CrTeBr monolayer, in which both the frustration ratio and the magnitude of in-plane anisotropy are very significant.

Next, we include the biquadratic interaction in the spin dynamics. The Hamiltonian reads $H = -\frac{1}{2} \sum_{i,j} J_{ij} (\mathbf{S}_i \cdot \mathbf{S}_j) - \frac{1}{2} B_1 \sum_{<i,j>} (\mathbf{S}_i \cdot \mathbf{S}_j)^2 - K_{\mathrm{MCA}} \sum_i (\mathbf{S}_i^z)^2 + E_{\mathrm{ddi}}$. Compared with Figs. 6(a)–6(d), the quantity of solitonlike configurations in Figs. 6(e) and 6(f) significantly decreases. This effect is confirmed by the spin dynamics using the VAMPIRE code [75], as shown in Fig. S5 in the Supplemental Material [60]. We note that all MnXZ and CrYZ monolayers show positive values of biquadratic interaction, which favors collinear spin configurations and suppresses the noncollinear magnetism [78].

Furthermore, we calculated the distribution of topological charge for each magnetization configuration as follows [31,79]:

$$Q = \frac{1}{4\pi} \int \mathbf{s} \cdot \left(\frac{\partial \mathbf{s}}{\partial x} \times \frac{\partial \mathbf{s}}{\partial y} \right) dx dy, \qquad (13)$$

where $\mathbf{s} = \mathbf{S}/|\mathbf{S}|$ is the three-component spin field. As shown in Figs. 7(a)–7(h), the biquadratic interaction greatly reduces the density of topological charge induced by frustration in MnPCl, CrTeI, MnAsBr, and CrTeBr. More appealingly, the areas with only one sign (positive or negative) of topological charge could be retained while biquadratic interaction is included. These results agree with previous studies in which biquadratic interaction could reduce the chaotic behavior of frustration-induced topological magnetism in the CrCl$_3$ monolayer [31]. Consequently, instead of decreasing, the total topological charge of CrTeBr increases while biquadratic interaction is included.

Moreover, we include all the isotropic HOI terms in the Hamiltonian. The relaxed spin configurations for MnPCl, CrTeI, MnAsBr, and CrTeBr are shown in Figs. 6(i)–6(l). From the Binet-Cauchy identity [80], $(\mathbf{A} \cdot \mathbf{B})(\mathbf{C} \cdot \mathbf{D}) = (\mathbf{A} \cdot \mathbf{D})(\mathbf{B} \cdot \mathbf{C}) + (\mathbf{A} \times \mathbf{C})(\mathbf{B} \times \mathbf{D})$, the four-site interaction F_1 can generate DMI-like impact on neighboring spins [14,40,50].

Additionally, different to the systems in previous reports [50,66], MnXZ monolayers exhibit significant negative three-site interaction Y_1, which could also lead to a competing effect among neighboring spins rather than forming the uudd spin configurations [44]. As shown in Figs. 6(i)–6(l) and 7(i)–7(l), high-Q bimerons can be induced in MnPCl and CrTeI. For MnPCl, CrTeI, MnAsBr, and CrTeBr, considering Heisenberg exchanges and all the isotropic HOI terms, the distribution of topological charge significantly increases compared with the cases in Figs. 6(e)–6(h) and 7(e)–7(h). Here, CrYZ monolayers show small values of three-site interaction Y_1; thus, biquadratic interaction B_1 dominates in CrTeI and CrTeBr. Therefore, the distributions of topological charge in Figs. 7(j)–7(l) are less dense than Figs. 7(b)–7(d).

2. Interplay between DMI, frustration, and HOI terms

Finally, we explore the interplay between DMI, frustration, and HOI terms for MnXZ and CrYZ monolayers. For the monolayers with larger DMI ratios, the frustration ratio $|J_3|/J_1$ increases in the sequence of CrSeI, CrTeI, MnAsBr, CrTeBr, and CrTeCl. To examine the interplay between DMI and frustration, we neglect the HOI terms in Eq. (1) for CrSeI, CrTeI, MnAsBr, CrTeBr, and CrTeCl; the relaxed magnetization configurations are shown in Figs. 8(a)–8(e), respectively. As the frustration ratio $|J_3|/J_1$ increases, the field-free spin configurations gradually evolve from skyrmions to coexistent wormlike domains and skyrmions and to spin-helix states with the areas of the so-called distorted spin spirals [81] or multi-band spin helix [82]. This trend is confirmed by spin dynamics with the VAMPIRE code in Fig. S6 in the Supplemental Material [60]. Especially, due to sizable d_z components, skyrmions in CrSeI and CrTeI show hybrid Bloch-Néel helicity [83] rather than typical Néel type.

Next, we include all the HOI terms in Eq. (1) for CrSeI, CrTeI, MnAsBr, CrTeBr, and CrTeCl. The relaxed spin configurations are shown in Figs. 8(f)–8(j), respectively. The evolving trends from skyrmions to distorted spin spirals are retained while HOI terms are considered. Interestingly, it is
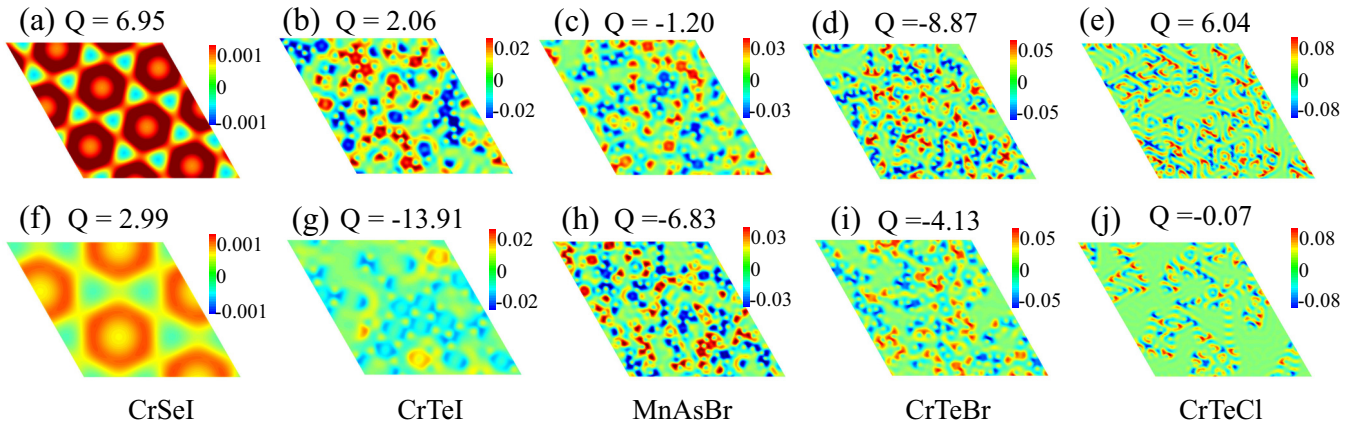
FIG. 9. The distribution of topological charge in a periodical nanodisk with 100×100 atoms in the absence of external field without isotropic higher-order interaction (HOI) for (a) CrSeI, (b) CrTeCl, (c) MnAsBr, (d) CrTeBr, and (e) CrTeCl, respectively. The distribution of topological charge in a periodical nanodisk with 100×100 atoms in the absence of external field for (f) CrSeI, (g) CrTeCl (h) MnAsBr, (i) CrTeBr, and (j) CrTeCl including DMI and isotropic HOI terms. Red (blue) in the color bars indicate positive (negative) topological charge densities, while green denotes zero topological charge density.

found that the distributions of topological charge become less dense for CrSeI, CrTeI, CrTeBr, and CrTeCl while HOI terms are considered, as shown in Figs. 9(a)–9(j). This impact mainly comes from biquadratic interaction, as the strengths of the three-site term Y_1 are weak in CrYZ monolayers. The only exceptional case is MnAsBr with larger Y_1. As shown in Figs. 9(c)–9(h), the density and the total number of topological charge increase while HOI terms are included for MnAsBr. Notably, the strength of F_1 of CrTeI reaches up to 0.98 meV, larger than that in MnAsBr, CrTeBr, and CrTeCl. The interplay between strong DMI and moderate frustration favors wormlike spin spirals, whereas four-spin-four-site interaction F_1 could generate a skyrmion state [14]. Hence, a skyrmion lattice (SKx)-like region can be formed in CrTeI when HOI terms are considered, as shown in Fig. 8(g).

Moreover, the regions of the so-called distorted spin spirals of CrTeCl in Figs. 8(e)–8(j) show zero topological charge, as demonstrated in Figs. 9(e)–9(j). Formed by the competition between strong frustration and DMI, the distorted spin spirals are very stable under external magnetic field [81,82]. Such nontopological spin configurations can convert to SKx under very strong magnetic field, which limits their potential applications [81,82].

Another interesting possibility is to explore topological magnetism in systems with weak DMI. Here, MnPBr and MnPCl monolayers show very weak DMI with the ratios of $|d_1^{\parallel}|/J_1 < 0.03$, which are far below the critical ratio of 0.08 [1,17,22]. Additionally, MnPBr and MnPCl exhibit weak or moderate frustration and sizable HOI terms. First, we neglect the HOI terms in Eq. (1) for MnPBr and MnPCl, the relaxed
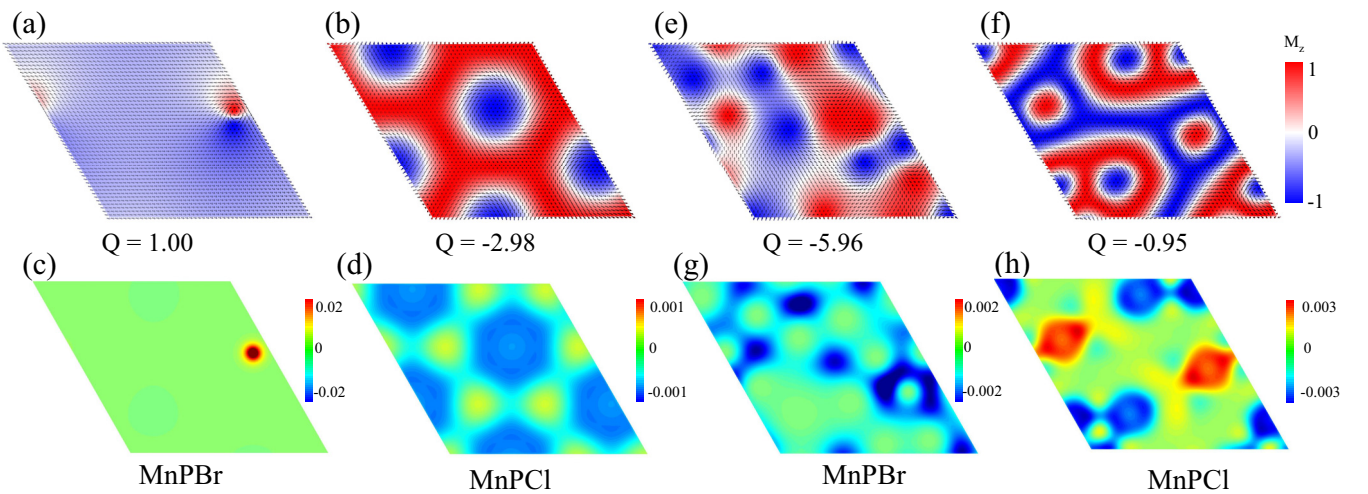

FIG. 10. The relaxed magnetization configuration in a periodical nanodisk with 100×100 atoms in the absence of external field without isotropic higher-order interaction (HOI) for (a) MnPBr and (b) MnPCl. The relaxed magnetization configuration in a periodical nanodisk with 100×100 atoms in the absence of external field for (e) MnPBr and (f) MnPCl, in which we included all the HOI terms. The color map indicates the out-of-plane spin components of Mn and Cr atoms. (c), (d), (g), and (h) are the respective schematics of topological charge distribution for (a), (b), (e), and (f), respectively. Red (blue) in the color bars indicate positive (negative) topological charge densities, while green denotes zero topological charge density.

spin configurations are shown in Figs. 10(a) and 10(b). Due to the interplay between frustration and very weak DMI, field-free bimerons and skyrmions can be found in MnPBr and MnPCl, respectively. Figures 10(e) and 10(f) plot the spin configurations with HOI terms for MnPBr and Mn-PCl. Field-free vortex-antivortex pairs are found in MnPBr, and skyrmions in the background of ferromagnetic domains emerge in MnPCl. Moreover, the topological charge distributions are enhanced while the HOI terms are included for both MnPBr and MnPCl, as shown in Figs. 10(c), 10(d) and 10(g), 10(h). As shown in Fig. S6 in the Supplemental Material [60], the spin configurations obtained by the VAMPIRE code for MnPBr and MnPCl are consistent with Figs. 10(a) and 10(b). Figure S6 in the Supplemental Material [60] shows that, with an exceptional case of MnAsI, field-free bimerons are also found in CrSeBr and CrSeCl.

IV. CONCLUSIONS

In summary, we predict a group Janus monolayers MnXZ (MnPCl, MnPBr, MnAsBr, and MnAsI) by using first-principles calculations. From calculating the DMI vectors and Heisenberg exchange parameters up to the NNNN in MnXZ and CrYZ ($Y = $ Se, Te; and $Z = $ Cl, Br, I) monolayers, we unveil the presence of various degrees of magnetic frustration from the NNNN antiferromagnetic exchanges, sizable DMI values, and isotropic HOIs for MnXZ and CrYZ. We confirm that various topological magnetism can be induced by magnetic frustration in MnPCl, CrTeI, MnAsBr, and CrTeBr even in the absence of DMI. HOI terms can act as modifiers to topological spin textures. Biquadratic interaction decreases the density as well as the chaotic behavior of distribution of topological charge. The three- and four-site interactions can moderately increase the density of topological charge. For CrSeI, CrTeI, MnAsBr, CrTeBr, and CrTeCl monolayers with larger DMI and increasing frustration ratios, the field-free spin textures gradually vary from skyrmions, common spin spirals to the so-called distorted spin spirals. For the monolayers with weak DMI such as MnPBr and MnPCl, topological spin textures can also be induced by the interplay between frustration and DMI. The isotropic HOI terms have a similar effect on the spin textures generated only by frustration and that induced by the interplay between frustration and DMI. Our work deepens the understanding of topological spin textures originating from the interplay among DMI, magnetic frustration, and biquadratic interaction and will pave a route toward chiral magnetism-based spintronics in 2D materials.

[1] A. Fert, V. Cros, and J. Sampaio, Skyrmions on the track, Nat. Nanotechnol. **8**, 152 (2013).

[2] A. Fert, N. Reyren, and V. Cros, Magnetic skyrmions: Advances in physics and potential applications, Nat. Rev. Mater. **2**, 17031 (2017).

[3] X. Z. Yu, Y. Onose, N. Kanazawa, J. H. Park, J. H. Han, Y. Matsui, N. Nagaosa, and Y. Tokura, Real-space observation of a two-dimensional skyrmion crystal, Nature (London) **465**, 901 (2010).

[4] R. Wiesendanger, Nanoscale magnetic skyrmions in metallic films and multilayers: A new twist for spintronics, Nat. Rev. Mater. **1**, 16044 (2016).

[5] N. Gao, S.-G. Je, M.-Y. Im, J. W. Choi, M. Yang, Q. Li, T. Y. Wang, S. Lee, H.-S. Han, K.-S. Lee *et al.*, Creation and annihilation of topological meron pairs in in-plane magnetized films, Nat. Commun. **10**, 5603 (2019).

[6] K.-W. Moon, J. Yoon, C. Kim, and C. Hwang, Existence of In-Plane Magnetic Skyrmion and Its Motion under Current Flow, Phys. Rev. Appl. **12**, 064054 (2019).

[7] X. Li, L. Shen, Y. Bai, J. Wang, X. Zhang, J. Xia, M. Ezawa, O. A. Tretiakov, X. Xu, and M. Mruczkiewicz, Bimeron clusters in chiral antiferromagnets, npj Comput. Mater. **6**, 169 (2020).

[8] I. Dzyaloshinsky, A thermodynamic theory of "weak" ferromagnetism of antiferromagnetics, J. Phys. Chem. Solids **4**, 241 (1958).

[9] T. Moriya, Anisotropic superexchange interaction and weak ferromagnetism, Phys. Rev. **120**, 91 (1960).

[10] A. Neubauer, C. Pfleiderer, B. Binz, A. Rosch, R. Ritz, P. G. Niklowitz, and P. Böni, Topological Hall Effect in the *A* Phase of Mnsi, Phys. Rev. Lett. **102**, 186602 (2009).

[11] B. Dupé, M. Hoffmann, C. Paillard, and S. Heinze, Tailoring magnetic skyrmions in ultra-thin transition metal films, Nat. Commun. **5**, 4030 (2014).

[12] O. Boulle, J. Vogel, H. Yang, S. Pizzini, D. de Souza Chaves, A. Locatelli, T. O. Menteş, A. Sala, L. D. Buda-Prejbeanu, and O. Klein, Room-temperature chiral magnetic skyrmions in ultrathin magnetic nanostructures, Nat. Nanotechnol. **11**, 449 (2016).

[13] A. Soumyanarayanan, M. Raju, A. G. Oyarce, A. K. Tan, M.-Y. Im, A. Petrović, P. Ho, K. Khoo, M. Tran, and C. Gan, Tunable room-temperature magnetic skyrmions in Ir/Fe/Co/Pt multilayers, Nat. Mater. **16**, 898 (2017).

[14] S. Heinze, K. Von Bergmann, M. Menzel, J. Brede, A. Kubetzka, R. Wiesendanger, G. Bihlmayer, and S. Blügel, Spontaneous atomic-scale magnetic skyrmion lattice in two dimensions, Nat. Phys. **7**, 713 (2011).

[15] H. Yang, A. Thiaville, S. Rohart, A. Fert, and M. Chshiev, Anatomy of Dzyaloshinskii-Moriya Interaction at Co/Pt Interfaces, Phys. Rev. Lett. **115**, 267210 (2015).

[16] M. Raju, A. Yagil, A. Soumyanarayanan, A. K. Tan, A. Almoalem, F. Ma, O. Auslaender, and C. Panagopoulos,

The evolution of skyrmions in Ir/Fe/Co/Pt multilayers and their topological Hall signature, Nat. Commun. **10**, 696 (2019).

[17] J. Liang, W. Wang, H. Du, A. Hallal, K. Garcia, M. Chshiev, A. Fert, and H. Yang, Very large Dzyaloshinskii-Moriya interaction in two-dimensional janus manganese dichalcogenides and its application to realize skyrmion states, Phys. Rev. B **101**, 184401 (2020).

[18] Q. Cui, J. Liang, Z. Shao, P. Cui, and H. Yang, Strain-tunable ferromagnetism and chiral spin textures in two-dimensional janus chromium dichalcogenides, Phys. Rev. B **102**, 094425 (2020).

[19] C. Xu, J. Feng, S. Prokhorenko, Y. Nahas, H. Xiang, and L. Bellaiche, Topological spin texture in janus monolayers of the chromium trihalides $Cr(I,X)_3$, Phys. Rev. B **101**, 060404(R) (2020).

[20] Y. Zhang, C. Xu, P. Chen, Y. Nahas, S. Prokhorenko, and L. Bellaiche, Emergence of skyrmionium in a two-dimensional $CrGe(Se, Te)_3$ Janus monolayer, Phys. Rev. B **102**, 241107(R) (2020).

[21] J. Liang, Q. Cui, and H. Yang, Electrically switchable Rashba-type Dzyaloshinskii-Moriya interaction and skyrmion in two-dimensional magnetoelectric multiferroics, Phys. Rev. B **102**, 220409(R) (2020).

[22] P. Li, Q. Cui, Y. Ga, J. Liang, and H. Yang, Large Dzyaloshinskii-Moriya interaction and field-free topological chiral spin states in two-dimensional alkali-based chromium chalcogenides, Phys. Rev. B **106**, 024419 (2022).

[23] Q. Cui, Y. Zhu, Y. Ga, J. Liang, P. Li, D. Yu, P. Cui, and H. Yang, Anisotropic Dzyaloshinskii–Moriya interaction and topological magnetism in two-dimensional magnets protected by $P\bar{4}m2$ crystal symmetry, Nano Lett. **22**, 2334 (2022).

[24] Y. Ga, Q. Cui, Y. Zhu, D. Yu, L. Wang, J. Liang, and H. Yang, Anisotropic Dzyaloshinskii-Moriya interaction protected by D_{2d} crystal symmetry in two-dimensional ternary compounds, npj Comput. Mater. **8**, 128 (2022).

[25] X. Yu, M. Mostovoy, Y. Tokunaga, W. Zhang, K. Kimoto, Y. Matsui, Y. Kaneko, N. Nagaosa, and Y. Tokura, Magnetic stripes and skyrmions with helicity reversals, Proc. Natl. Acad. Sci. USA **109**, 8856 (2012).

[26] T. Kurumaji, T. Nakajima, M. Hirschberger, A. Kikkawa, Y. Yamasaki, H. Sagayama, H. Nakao, Y. Taguchi, T.-h. Arima, and Y. Tokura, Skyrmion lattice with a giant topological Hall-effect in a frustrated triangular-lattice magnet, Science **365**, 914 (2019).

[27] Y. Yasui, C. J. Butler, N. D. Khanh, S. Hayami, T. Nomoto, T. Hanaguri, Y. Motome, R. Arita, T.-h. Arima, Y. Tokura *et al.*, Imaging the coupling between itinerant electrons and localised moments in the centrosymmetric skyrmion magnet $GdRu_2Si_2$, Nat. Commun. **11**, 5925 (2020).

[28] N. D. Khanh, T. Nakajima, X. Yu, S. Gao, K. Shibata, M. Hirschberger, Y. Yamasaki, H. Sagayama, H. Nakao, L. Peng *et al.*, Nanometric square skyrmion lattice in a centrosymmetric tetragonal magnet, Nat. Nanotechnol. **15**, 444 (2020).

[29] D. Amoroso, P. Barone, and S. Picozzi, Spontaneous skyrmionic lattice from anisotropic symmetric exchange in a Ni-halide monolayer, Nat. Commun. **11**, 5784 (2020).

[30] K. Riedl, D. Amoroso, S. Backes, A. Razpopov, T. P. T. Nguyen, K. Yamauchi, P. Barone, S. M. Winter, S. Picozzi, and

R. Valentí, Microscopic origin of magnetism in monolayer $3d$ transition metal dihalides, Phys. Rev. B **106**, 035156 (2022).

[31] M. Augustin, S. Jenkins, R. F. Evans, K. S. Novoselov, and E. J. Santos, Properties and dynamics of meron topological spin textures in the two-dimensional magnet $CrCl_3$, Nat. Commun. **12**, 1 (2021).

[32] X. Lu, R. Fei, L. Zhu, and L. Yang, Meron-like topological spin defects in monolayer $CrCl_3$, Nat. Commun. **11**, 4724 (2020).

[33] T. Okubo, S. Chung, and H. Kawamura, Multiple-Q States and the Skyrmion Lattice of the Triangular-Lattice Heisenberg Antiferromagnet Under Magnetic Fields, Phys. Rev. Lett. **108**, 017206 (2012).

[34] C. D. Batista, S.-Z. Lin, S. Hayami, and Y. Kamiya, Frustration and chiral orderings in correlated electron systems, Rep. Prog. Phys. **79**, 084504 (2016).

[35] S. Hayami, S.-Z. Lin, and C. D. Batista, Bubble and skyrmion crystals in frustrated magnets with easy-axis anisotropy, Phys. Rev. B **93**, 184413 (2016).

[36] A. Leonov and M. Mostovoy, Multiply periodic states and isolated skyrmions in an anisotropic frustrated magnet, Nat. Commun. **6**, 8275 (2015).

[37] A. Leonov and M. Mostovoy, Edge states and skyrmion dynamics in nanostripes of frustrated magnets, Nat. Commun. **8**, 14394 (2017).

[38] S. Hayami and Y. Motome, Topological spin crystals by itinerant frustration, J. Phys.: Condens. Matter **33**, 443001 (2021).

[39] M. Miyata, J.-i. Ohe, and G. Tatara, Topological Charge Control of Skyrmion Structure in Frustrated Magnets by Circularly Polarized Light, Phys. Rev. Appl. **18**, 014075 (2022).

[40] M. Hoffmann and S. Blügel, Systematic derivation of realistic spin models for beyond-Heisenberg solids, Phys. Rev. B **101**, 024418 (2020).

[41] S. Haldar, S. von Malottki, S. Meyer, P. F. Bessarab, and S. Heinze, First-principles prediction of sub-10-nm skyrmions in Pd/Fe bilayers on Rh(111), Phys. Rev. B **98**, 060413(R) (2018).

[42] A. S. Varentcova, S. von Malottki, M. N. Potkina, G. Kwiatkowski, S. Heinze, and P. F. Bessarab, Toward room-temperature nanoscale skyrmions in ultrathin films, npj Comput. Mater. **6**, 193 (2020).

[43] N. Romming, H. Pralow, A. Kubetzka, M. Hoffmann, S. von Malottki, S. Meyer, B. Dupé, R. Wiesendanger, K. von Bergmann, and S. Heinze, Competition of Dzyaloshinskii-Moriya and Higher-Order Exchange Interactions in Rh/Fe Atomic Bilayers on Ir (111), Phys. Rev. Lett. **120**, 207201 (2018).

[44] A. Krönlein, M. Schmitt, M. Hoffmann, J. Kemmer, N. Seubert, M. Vogt, J. Küspert, M. Böhme, B. Alonazi, J. Kügel *et al.*, Magnetic Ground State Stabilized by Three-Site Interactions: Fe/Rh (111), Phys. Rev. Lett. **120**, 207202 (2018).

[45] J. Spethmann, S. Meyer, K. von Bergmann, R. Wiesendanger, S. Heinze, and A. Kubetzka, Discovery of Magnetic Single- and Triple-**q** states in Mn/Re (0001), Phys. Rev. Lett. **124**, 227203 (2020).

[46] A. Kartsev, M. Augustin, R. F. L. Evans, K. S. Novoselov, and E. J. G. Santos, Biquadratic exchange interactions in two-dimensional magnets, npj Comput. Mater. **6**, 150 (2020).

[47] D. A. Wahab, M. Augustin, S. M. Valero, W. Kuang, S. Jenkins,

E. Coronado, I. V. Grigorieva, I. J. Vera-Marun, E. Navarro-Moratalla, R. F. L. Evans *et al.*, Quantum rescaling, domain metastability, and hybrid domain-walls in 2D CrI_3 Magnets, Adv. Mater. **33**, 2004138 (2021).

[48] J. Y. Ni, X. Y. Li, D. Amoroso, X. He, J. S. Feng, E. J. Kan, S. Picozzi, and H. J. Xiang, Giant Biquadratic Exchange in 2D Magnets and Its Role in Stabilizing Ferromagnetism of $NiCl_2$ Monolayers, Phys. Rev. Lett. **127**, 247204 (2021).

[49] M. Strungaru, M. Augustin, and E. J. G. Santos, Ultrafast laser-driven topological spin textures on a 2D magnet, npj Comput. Mater. **8**, 169 (2022).

[50] C. Xu, X. Li, P. Chen, Y. Zhang, H. Xiang, and L. Bellaiche, Assembling diverse skyrmionic phases in Fe_3GeTe_2, monolayers, Adv. Mater. **34**, 2107779 (2022).

[51] S. Laref, K.-W. Kim, and A. Manchon, Elusive Dzyaloshinskii-Moriya interaction in monolayer Fe_3GeTe_2, Phys. Rev. B **102**, 060402(R) (2020).

[52] J. Xiao, D. Legut, W. Luo, H. Guo, X. Liu, R. Zhang, and Q. Zhang, Modulating superexchange strength to achieve robust ferromagnetic couplings in two-dimensional semiconductors, Phys. Rev. B **101**, 014431 (2020).

[53] Y. Hou, F. Xue, L. Qiu, Z. Wang, and R. Wu, Multifunctional two-dimensional van der Waals Janus magnet Cr-based dichalcogenide halides, npj Comput. Mater. **8**, 120 (2022).

[54] G. Kresse and J. Hafner, *Ab initio* molecular dynamics for liquid metals, Phys. Rev. B **47**, 558 (1993).

[55] G. Kresse and J. Furthmüller, Efficient iterative schemes for *ab initio* total-energy calculations using a plane-wave basis set, Phys. Rev. B **54**, 11169 (1996).

[56] G. Kresse and J. Furthmüller, Efficiency of *ab-initio* total energy calculations for metals and semiconductors using a plane-wave basis set, J. Comput. Mater. Sci. **6**, 15 (1996).

[57] Y. Wang and J. P. Perdew, Correlation hole of the spin-polarized electron gas, with exact small-wave-vector and high-density scaling, Phys. Rev. B **44**, 13298 (1991).

[58] G. Kresse and D. Joubert, From ultrasoft pseudopotentials to the projector augmented-wave Method, Phys. Rev. B **59**, 1758 (1999).

[59] A. Togo, L. Chaput, and I. Tanaka, Distributions of phonon lifetimes in Brillouin zones, Phys. Rev. B **91**, 094306 (2015).

[60] See Supplemental Material at http://link.aps.org/supplemental/10.1103/PhysRevB.107.054408 for (1) phonon spectrum of MnAsBr, MnAsI, MnPCl, and MnPBr monolayers.; (2) non-SOC and SOC-included spin spirals and in-plane DMI spectrum for all the Mn*XZ* and Cr*YZ* monolayers; (3) SOC-included spin spirals and out-of-plane DMI spectrum for all the Mn*XZ* and Cr*YZ* monolayers; (4) computational detail of determined HOIs for all the Mn*XZ* and Cr*YZ* monolayers; and (5) and (6) atomistic spin model simulations by VAMPIRE code.

[61] S. Brinker, M. D. Santos Dias, and S. Lounis, The chiral biquadratic pair interaction, New J. Phys. **21**, 083015 (2019).

[62] S. Lounis, Multiple-scattering approach for multi-spin chiral magnetic interactions: Application to the one-and two-dimensional Rashba electron gas, New J. Phys. **22**, 103003 (2020).

[63] A. Lászlóffy, L. Rózsa, K. Palotás, L. Udvardi, and L. Szunyogh, Magnetic structure of monatomic Fe chains on Re (0001): Emergence of chiral multispin interactions, Phys. Rev. B **99**, 184430 (2019).

[64] S. Brinker, M. D. Santos Dias, and S. Lounis, Prospecting chiral multisite interactions in prototypical magnetic systems, Phys. Rev. Res. **2**, 033240 (2020).

[65] S. Mankovsky, S. Polesya, and H. Ebert, Extension of the standard Heisenberg Hamiltonian to multispin exchange interactions, Phys. Rev. B **101**, 174401 (2020).

[66] M. Gutzeit, A. Kubetzka, S. Haldar, H. Pralow, M. A. Goerzen, R. Wiesendanger, S. Heinze, and K. von Bergmann, Nano-scale collinear multi-*Q* states driven by higher-order interactions, Nat. Commun. **13**, 5764 (2022).

[67] L. M. Sandratskii, Insight into the Dzyaloshinskii-Moriya interaction through first-principles study of chiral magnetic structures, Phys. Rev. B **96**, 024450 (2017).

[68] H. Yang, J. Liang, and Q. Cui, First-principles calculations for Dzyaloshinskii–Moriya interaction, Nat. Rev. Phys. **5**, 43 (2022).

[69] M. Heide, G. Bihlmayer, and S. Blügel, Describing Dzyaloshinskii–Moriya spirals from first principles, Phys. B: Condens. Matter **404**, 2678 (2009).

[70] L. Sandratskii, Symmetry analysis of electronic states for crystals with spiral magnetic order. I. General properties, J. Phys.: Condens. Matter **3**, 8565 (1991).

[71] B. Zimmermann, G. Bihlmayer, M. Böttcher, M. Bouhassoune, S. Lounis, J. Sinova, S. Heinze, S. Blügel, and B. Dupé, Comparison of first-principles methods to extract magnetic parameters in ultrathin films: Co/Pt(111), Phys. Rev. B **99**, 214426 (2019).

[72] S. Paul, S. Haldar, S. von Malottki, and S. Heinze, Role of higher-order exchange interactions for skyrmion stability, Nat. Commun. **11**, 4756 (2020).

[73] P. B. Ndiaye, A. Abbout, V. M. L. D. P. Goli, and A. Manchon, Quantum anomalous Hall effect and Anderson-chern insulating regime in the noncollinear antiferromagnetic 3*Q* state, Phys. Rev. B **100**, 144440 (2019).

[74] G. P. Müller, M. Hoffmann, C. Dißelkamp, D. Schürhoff, S. Mavros, M. Sallermann, N. S. Kiselev, H. Jónsson, and S. Blügel, Spirit: Multifunctional framework for atomistic spin simulations, Phys. Rev. B **99**, 224414 (2019).

[75] R. F. Evans, W. J. Fan, P. Chureemart, T. A. Ostler, M. O. Ellis, and R. W. Chantrell, Atomistic spin model simulations of magnetic nanomaterials, J. Phys.: Condens. Matter **26**, 103202 (2014).

[76] C. Moutafis, S. Komineas, and J. Bland, Dynamics and switching processes for magnetic bubbles in nanoelements, Phys. Rev. B **79**, 224429 (2009).

[77] F. S. Yasin, L. Peng, R. Takagi, N. Kanazawa, S. Seki, Y. Tokura, and X. Yu, Bloch lines constituting antiskyrmions captured via differential phase contrast, Adv. Mater. **32**, 2004206 (2020).

[78] S. Hayami, R. Ozawa, and Y. Motome, Effective bilinear-biquadratic model for noncoplanar ordering in itinerant magnets, Phys. Rev. B **95**, 224424 (2017).

[79] B. Berg and M. Lüscher, Definition and statistical distributions of a topological number in the lattice O(3) σ-model, Nucl. Phys. B **190**, 412 (1981).

[80] E. W. Weisstein, *CRC Concise Encyclopedia of Mathematics* (Chapman and Hall/CRC, New York, 2002).

[81] T. T. Mutter, A. O. Leonov, and K. Inoue, Skyrmion instabilities and distorted spiral states in a frustrated chiral magnet, Phys. Rev. B **100**, 060407(R) (2019).

[82] H. Yuan, O. Gomonay, and M. Kläui, Skyrmions and multisublattice helical states in a frustrated chiral magnet, Phys. Rev. B **96**, 134415 (2017).

[83] P. Olleros-Rodríguez, R. Guerrero, J. Camarero, O. Chubykalo-Fesenko, and P. Perna, Intrinsic mixed Bloch–Néel character and chirality of skyrmions in asymmetric epitaxial trilayers, ACS Appl. Mater. Interfaces **12**, 25419 (2020).